



## Source Functions and Path Effects from Earthquakes in the Farallon Transform Fault Region, Gulf of California, Mexico that Occurred on October 2013

RAÚL R. CASTRO,<sup>1</sup> JOANN M. STOCK,<sup>2</sup> EGILL HAUKSSON,<sup>2</sup> and ROBERT W. CLAYTON<sup>2</sup>

**Abstract**—We determined source spectral functions,  $Q$  and site effects using regional records of body waves from the October 19, 2013 ( $M_w = 6.6$ ) earthquake and eight aftershocks located 90 km east of Loreto, Baja California Sur, Mexico. We also analyzed records from a foreshock with magnitude 3.3 that occurred 47 days before the mainshock. The epicenters of this sequence are located in the south-central region of the Gulf of California (GoC) near and on the Farallon transform fault. This is one of the most active regions of the GoC, where most of the large earthquakes have strike–slip mechanisms. Based on the distribution of the aftershocks, the rupture propagated northwest with a rupture length of approximately 27 km. We calculated 3-component P- and S-wave spectra from ten events recorded by eleven stations of the Broadband Seismological Network of the GoC (RESBAN). These stations are located around the GoC and provide good azimuthal coverage (the average station gap is  $39^\circ$ ). The spectral records were corrected for site effects, which were estimated calculating average spectral ratios between horizontal and vertical components (HVSr method). The site-corrected spectra were then inverted to determine the source functions and to estimate the attenuation quality factor  $Q$ . The values of  $Q$  resulting from the spectral inversion can be approximated by the relations  $Q_p = 48.1 \pm 1.1f^{0.88 \pm 0.04}$  and  $Q_s = 135.4 \pm 1.1f^{0.58 \pm 0.03}$  and are consistent with previous estimates reported by Vidales-Basurto et al. (Bull Seism Soc Am 104:2027–2042, 2014) for the south-central GoC. The stress drop estimates, obtained using the  $\omega^2$  model, are below 1.7 MPa, with the highest stress drops determined for the mainshock and the aftershocks located in the ridge zone. We used the values of  $Q$  obtained to recalculate source and site effects with a different spectral inversion scheme. We found that sites with low S-wave amplification also tend to have low P-wave amplification, except for stations BAHB, GUYB and SFQB, located on igneous rocks, where the P-wave site amplification is higher.

**Key words:** Earthquakes in the Gulf of California, source and path effects, Farallon transform fault.

### 1. Introduction

The plate boundary between North America and the Pacific plates cuts across the Gulf of California. The present style of rifting started at  $\sim 6$  Ma (Atwater and Stock 1998), and the deformation in this region is governed by oblique faults in the north and transform faults in the south (Fenby and Gastil 1991; Nagy and Stock 2000).

The October 19, 2013 ( $M_w = 6.6$ ) earthquake was located by the National Seismological Service of Mexico (SSN) at 90 km east of Loreto, Baja California Sur, Mexico, near the Farallon transform fault (Fig. 1). This event and eight aftershocks with magnitudes ( $M_w$ ) ranging from 1.9 to 4.4 occurred in one of the most seismically active regions of the Gulf of California. The aftershocks were located in the Carmen basin, between the Carmen and Farallon transform faults. The focal mechanism of the mainshock (Fig. 2), taken from the GCMT catalog, exhibits right-lateral strike–slip motion on a NW-striking fault (strike =  $222^\circ$ , dip =  $86^\circ$ , rake =  $6^\circ$ ). Most of the aftershocks (Figs. 1, 2) are located within 27 km northwest of the epicenter of the mainshock, suggesting unilateral rupture to the northwest. The location of the centroid, where the maximum slip of the fault occurs, is also to the northwest (azimuth =  $334^\circ$ ) of the epicenter reported by the SSN.

The large earthquakes in this region typically accommodate strike–slip movement (Goff et al. 1987; Castro et al. 2011a), but normal faulting events occur near the ends of the spreading centers where they connect to transform faults. Previous events on the Farallon transform fault include the  $M_w = 7.0$  of December 9, 1901 (Pacheco and Sykes 1992); the  $M_w = 6.2$  of August 28, 1995 (Tanioka and Ruff

<sup>1</sup> Departamento de Sismología, CICESE, Carretera Ensenada-Tijuana 3918, 22860 Ensenada, Baja California, Mexico. E-mail: raul@cicese.mx

<sup>2</sup> Seismological Laboratory, Caltech, 1200 E. California Blvd., Pasadena, CA 91125, USA.

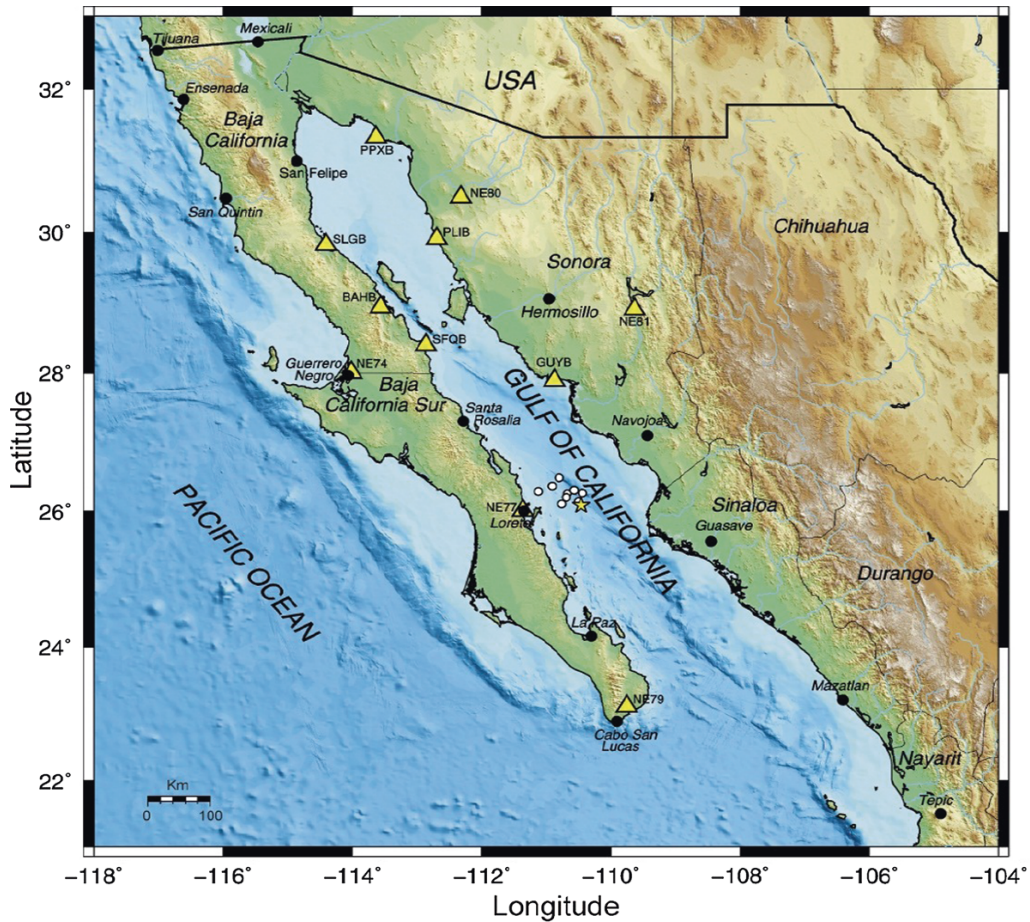


Figure 1

Distribution of stations of the RESBAN network (triangles), location of main event (star) and aftershocks analyzed (circles). This map was generated using Generic Mapping Tools (Wessel and Smith 1998)

1997); and the February 22, 2005 event, a moderate magnitude earthquake ( $M_w = 5.5$ ) that occurred 48 km southeast of the October 19, 2013 epicenter. Rodriguez-Lozoya et al. (2008) calculated the focal mechanism of this event and found a right-lateral strike-slip fault plane solution. The southern region of the Gulf of California (GoC), where these earthquakes were located, is characterized by thin oceanic crust (Zhang et al. 2007), which suggests that longer rupture lengths may be expected for a given magnitude, than those from events in other tectonic environments with thicker crust and deeper rupture.

A few studies of source parameters have been made from earthquakes in the GoC, for instance, Munguía et al. (1977) studied the aftershock

sequence of the July 8, 1975 Canal de Ballenas ( $M_S = 6.5$ ) earthquake; Goff et al. (1987) calculated earthquake source mechanisms of events that occurred on transform faults; Rebollar et al. (2001) estimated source parameters of a  $M_S = 5.5$  earthquake that occurred in the Delfin basin, northern GoC; and López-Pineda and Rebollar (2005) determined the source characteristics of the March 12, 2003 ( $M_w = 6.2$ ) Loreto earthquake and 20 other earthquakes with magnitude greater than five that occurred in different parts of the GoC. More recently, Castro et al. (2011b) studied the August 3, 2009 ( $M_w = 6.9$ ) Canal de Ballenas earthquake and its aftershocks. In general, the stress drops of the events in the GoC tend to be low; for instance, the average

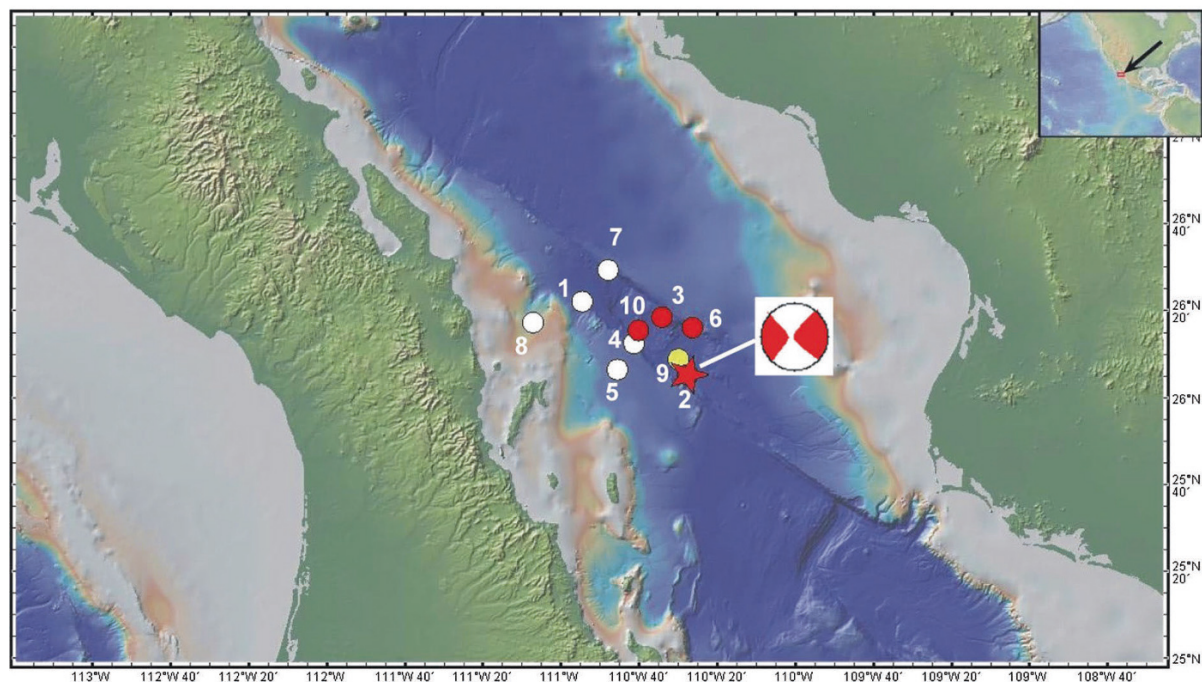


Figure 2

Epicenters of the 2013 sequence. The focal mechanism shown is of the main event and was taken from the GCMT catalog. The *white circle* marked with the number 1 is an  $M = 3.3$  foreshock recorded on September 2, 2013 (47 days before the main event). *Red circles* indicate events with stress drop ( $\Delta\sigma$ ) greater than 1.0 MPa, *yellow circles* events with  $0.5 \leq \Delta\sigma < 1.0$  MPa, and *white circles* events with  $\Delta\sigma < 0.5$  MPa. The topography and bathymetry are from GeoMap App

stress drop of the earthquakes analyzed by López-Pineda and Rebolgar (2005) is 0.25 MPa. For the Canal de Ballenas region, Munguía et al. (1977) estimated a stress drop of 0.4 MPa for the July 1975 ( $M_S = 6.5$ ) event, and Castro et al. (2011b) calculated a stress drop of 2.2 MPa for the August 2009 ( $M_w = 6.9$ ) event.

Here, we determine source parameters and path characteristics of the October 19, 2013 ( $M_w = 6.6$ ) earthquake sequence and a  $M_w = 3.3$  earthquake that occurred 47 days before the main event in the rupture area.

## 2. Tectonic Setting

The Gulf of California is an oblique rift system with short spreading centers connected by transform faults. The peninsula of Baja California, located on the west side of the GoC, moves with the Pacific plate

with approximately 48 mm/year of spreading across the GoC (Lizarralde et al. 2007). Between about 12 and 3.5 Ma Baja California was a rigid micro-plate bounded by the displacement between the Pacific and North America plates. The dominant extensional faults in the Gulf Extensional Province strike NNW, but the exact direction of extension is unknown (Stock and Hodges 1989). In the central-south GoC, south of Canal de Ballenas (below 29°N), the plate boundary consists of a series of en echelon transform fault zones. The transform faults between Delfín and Carmen basins have generated 60 % of the plate boundary earthquakes with  $M_S > 6$  (Goff et al. 1987).

Several significant earthquakes have occurred along the Farallon–Carmen transform faults system in the past. Figure 3 shows the location of earthquakes with  $M_S > 5.8$  reported in this region. The 1901  $M_S = 7.0$  earthquake (Pacheco and Sykes 1992) is the biggest event instrumentally located in the GoC, and the epicenter is on the southeastern end of



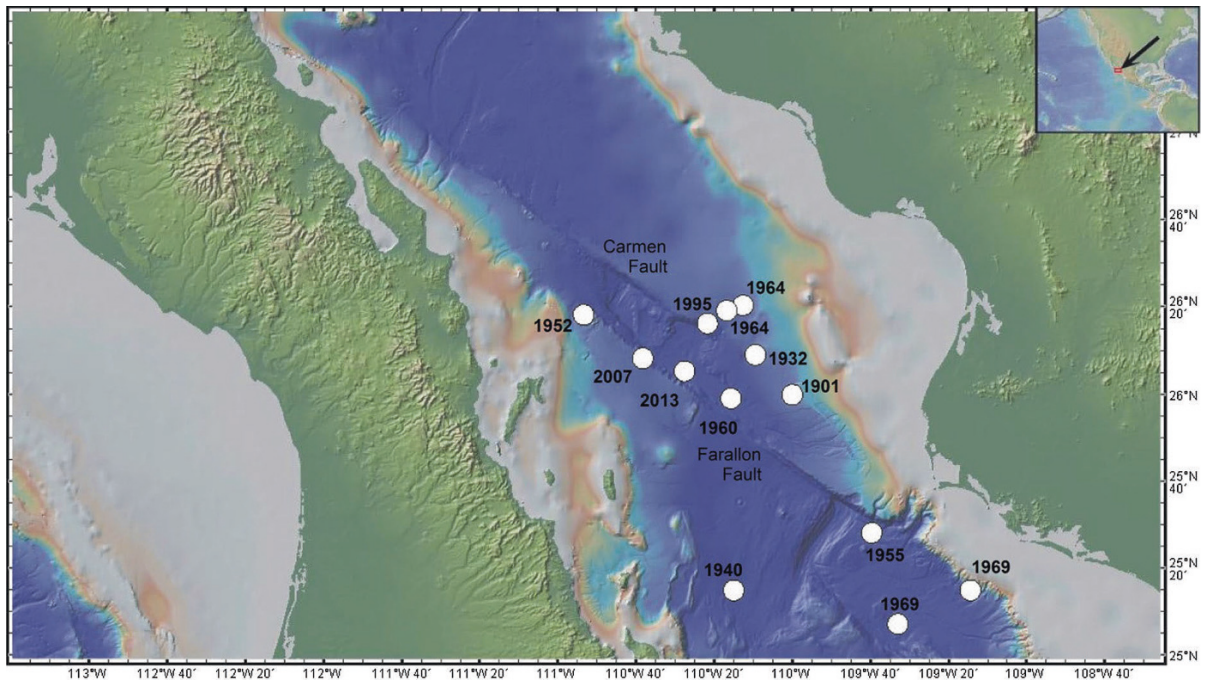


Figure 3

Historical seismicity within the Farallon transform fault region, only events with  $M_S > 5.8$  are shown (Table 1). The 1901 earthquake, the biggest of all, has a magnitude  $M_w = 7.0$  (Pacheco and Sykes 1992). The location of the 2013 ( $M_w = 6.6$ ) event was taken from the Mexican National Seismological Service (SSN) catalog. The topography and bathymetry are from GeoMap App

Table 1

Historical earthquakes in the Farallon transform fault region taken from Pacheco and Sykes (1992) (reference 1), the ISC catalog (reference 2) and Goff et al. (1987) (reference 3)

Date	Time	Lat	Lon	Depth	Mag ( $M_S$ )	References
1901-12-09	02:12	26.00	-110.00	-	7.0	1
1932-07-12	19:24	26.15	-110.16	10.0	6.8	2
1940-06-03	18:05	25.25	-110.25	35.0	6.2	2
1952-11-07	20:55	26.30	-110.89	15.0	6.3	2
1955-04-05	15:09	25.47	-109.66	15.0	6.5	2
1960-03-31	19:56	25.99	-110.26	15.0	5.8	2
1964-07-05	19:08	26.34	-110.21	-	6.3	3
1964-07-06	02:14	26.32	-110.28	-	6.6	3
1969-08-17	20:13	25.25	-109.24	-	6.5 ( $M_w$ )	3
1969-08-17	20:15	25.12	-109.55	-	6.6	3
1995-08-28	10:46	26.27	-110.36	12.2	6.5	2
2007-03-13	02:59	26.14	-110.64	10.0	5.8	2

Carmen fault. Tanioka and Ruff (1997) studied the source function of the 1995 ( $M_w = 6.2$ ) earthquake, which is also located on the Carmen fault together with the 1964 and 1932 earthquakes (Fig. 3). The earthquakes that occurred in 1952, 1955, 1960, 1969,

2007 and 2013 (Table 1) are located on the Farallon fault. The location of the 2013 ( $M_w = 6.6$ ) event in Fig. 3 was taken from the Mexican National Seismological Service catalog. The epicenter of the 1940 earthquake was probably mislocated, because it is

more than 30 km away from the closest active fault, and the epicenters in the GoC reported by ISC can have errors in the order of  $\sim 50$  km (Sumy et al. 2013). It is likely that the 1940 event is on the Pescadero fault together with the 1969 event.

A more detailed review of current bathymetric data helps to place the previous seismicity, and the 2013 earthquake sequence, in context. The 2013 earthquakes are within and near the Del Carmen Basin area of the Pacific–North America plate boundary in the Gulf of California (Figs. 2, 3). This spreading segment lies between the wider and better studied Guaymas Basin and Farallon Basin segments. In this region, the seismic velocity structure is likely to be complicated due to the irregular juxtaposition of continental and oceanic blocks. The crust of these central Gulf basins is inferred to comprise a variable mix of sediments and nascent oceanic crust lacking the abyssal hill fabric and marine magnetic reversal patterns characteristic of the southern Gulf of California basins and East Pacific Rise (EPR) (Lonsdale 1989). From crustal-scale seismic profiles of the Guaymas, Alarcon, and northern EPR segments, Lizarralde et al. (2007) identified the Continent–Ocean transition as a gradient in Moho depth and a lateral increase in  $V_p$ . Their results indicate that in the Guaymas basin, a 280-km-width of new igneous crust formed since ca. 6 Ma. The width of newly accreted oceanic crust in the Del Carmen and Farallon segments is not well constrained, but is probably  $<280$  km, because these segments include a wider zone of extended, partially submerged, continental crust in the Baja California continental borderland (Nava-Sánchez et al. 2001). In addition, the small Del Carmen basin is a younger offset in the plate boundary system; it appears to have formed along the transform offset separating the Guaymas and Farallon basins after those segments were already well established.

To relate the seismicity to the modern plate boundary geometry, we obtained multibeam data files from the IEDA Marine Geoscience Data System (Carbotte et al. 2004; <http://www.marine-geo.org>) for cruises AT15-31, DANA07RR, MOCE05MV, AT03-L46, and EW0210. We combined these multibeam data files using the software MB-System (Caress and

Chayes 2014) (<http://www.mbari.org/data/mbsystem>) to produce a detailed bathymetric map of the study area, and used it to make the following measurements and observations.

Along an NW–SE profile parallel to plate motion, the Del Carmen basin is a 70-km-wide bathymetric low with basin shoulders at ca. 1700 m water depth. This low contains three sub-basins: two in the center and on the SE side of the basin reaching 2300 m water depth and a third one, on the NW side of the basin, with a 14-km-long, 3-km-wide flat-bottomed trough reaching 2800 m water depth. Multibeam bathymetry suggests that this narrow trough, trending N32°E, represents the modern plate boundary, connecting at its northern end to the Carmen transform fault which has a strike here of N61°W. Southeastward from this trough, the Farallon transform fault system extends 130 km SE to the Farallon basin, but in two different segments with changing character along strike: an irregular zone in the northwestern 60 km and, then, a straight, more linear scarp for the southeastern 70 km. In detail, the irregular northwestern section of the Farallon transform fault system is characterized by a zigzag pattern of bathymetric scarps trending N47°W, N24°W, N50°W, and N25°W. The overall oblique orientation, compared to the N61°W Carmen transform fault, indicates that there are likely multiple active structures, and a broad zone of deformation, accommodating extension within and outside of the region of the Del Carmen basin. The 2013 earthquake sequence appears to be confined to the irregular northern zone of the Farallon transform fault and to the adjacent Del Carmen basin.

Sumy et al. (2013) relocated events in the Guaymas–Del Carmen basins from October 2005 to October 2006 using wave arrivals from an array of ocean-bottom seismographs deployed as part of the Sea of Cortez Ocean Bottom Array (SCOBA) experiment and onshore stations of the Network of Autonomously Recording Seismographs (NARS)-Baja array. Figure 4 shows only epicenters relocated by Sumy et al. (2013) between 24.5°N and 28°N, in the Guaymas basin and south. These well-located epicenters seem to concentrate near the spreading zones between the transform faults.

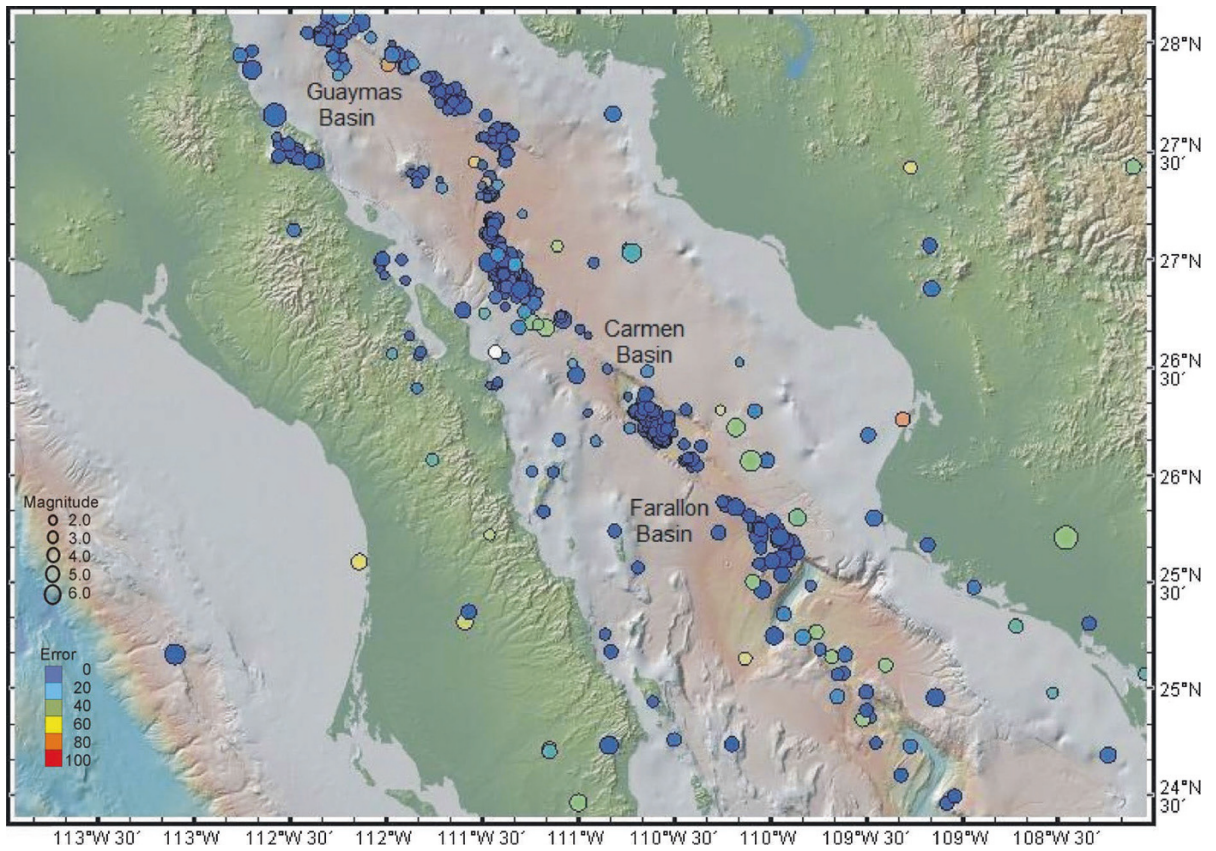


Figure 4

Epicenters relocated by Sumy et al. (2013) in the Guaymas—Del Carmen—Farallon basins from October 2005 to October 2006 using an array of ocean-bottom seismographs deployed as part of the Sea of Cortez Ocean Bottom Array (SCOoba) experiment and onshore stations of the Network of Autonomously Recording Seismographs (NARS)-Baja array. The topography and bathymetry are from GeoMap App. The size of the circle is proportional to the magnitude of the event and the color is proportional to the location error (*blue* low error; *red* high error)

Table 2

*Earthquake coordinates of the 2013 seismic sequence reported by the National Seismological Service (SSN) of the Instituto de Geofísica, UNAM*

Event no.	Date Y/M/D	Origin time hour:minute	Latitude N	Longitude W	Depth (km)
1	2013/09/02	19:50	26.37	110.91	16
2	2013/10/19	17:54	26.09	110.46	14
3	2013/10/19	22:14	26.26	110.67	16
4	2013/10/19	23:32	26.21	110.69	16
5	2013/10/20	04:19	26.11	110.76	–
6	2013/10/20	06:20	26.27	110.44	–
7	2013/10/20	08:18	26.49	110.80	16
8	2013/10/20	08:32	26.29	111.12	15
9	2013/10/20	12:01	26.15	110.50	16
10	2013/10/31	15:08	26.31	110.57	23



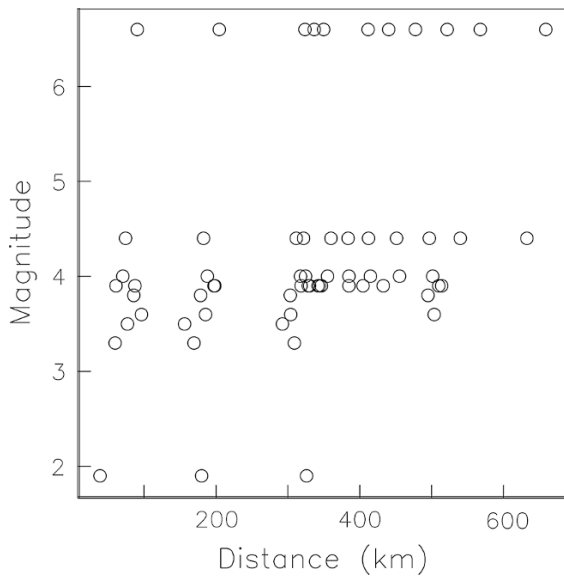


Figure 5

Epicentral distance distribution versus magnitude of the earthquakes analyzed

### 3. Data and Method

The dataset consists of 3-component waveforms from 11 stations (Fig. 1) of the broadband network RESBAN (*Red Sismologica de Banda Ancha del Golfo de California*) that recorded 10 moderate-size earthquakes (Table 2). The events analyzed have  $M_w$  magnitudes ranging from 1.9 to 6.6 and epicentral distances between 30 and 670 km (Fig. 5). The RESBAN stations are equipped with Guralp CMG-40T or CMG-3ESP digital three-component seismometers with a GPS and 24-bit Guralp digitizer. These broadband instruments are set to record earthquakes at a rate of 20 samples per second. Two of the stations (BAHB and GUYB) have Streckeisen STS-2 sensors and Reftek DAS 130 recorders that sample 100 samples per second. Figure 6 shows a sample of horizontal component waveforms from the mainshock (event 2 in Table 2). We consider that the 20 Hz sampling (10 Hz Nyquist) is high enough for our analyses, because only one of the earthquakes analyzed (event 8) has a magnitude  $M < 3$ . During the 2010–2012 Canterbury earthquake sequence, Van Houtte et al. (2014) show that events with  $M > 3$  tend to have corner frequencies  $f_c < 10$  Hz. Transform fault earthquakes with magnitudes between 5.5 and

7.1 tend to have even lower corner frequencies,  $0.07 < f_c < 0.2$  Hz (Stein and Pelayo 1991).

All the records were corrected for instrument response and baseline-corrected by subtracting the mean, and we choose time windows containing clear P- and S-wave arrivals to calculate Fourier acceleration spectra of the signals. We selected the beginning of the window about 1 s before the first phase arrival and the end a few seconds after the peak amplitude. For the P wave, the time window ends before the S-wave arrival and for the S wave, before the surface waves arrive. The window lengths vary depending on the epicentral distance and are typically 4–38 s for P waves and 6–112 s for S waves. The beginning and the end of the time windows were tapered with a 5 % cosine taper before the Fourier transform was calculated. The spectral amplitudes were smoothed using a variable frequency band of  $\pm 25$  % over 21 predefined central frequencies between 0.10 and 10.00 Hz, equidistant on a logarithmic scale. The spectral amplitudes at the central frequency selected are the average amplitude within the corresponding frequency band with the constraint that the total energy of the original spectrum is conserved (e.g., Castro et al. 1990). For further analysis, we inspected the spectral amplitudes to select frequency bands above the noise level, and we use spectral amplitudes with signal-to-noise ratio above a factor of two. We differentiated the records in the frequency domain to obtain acceleration spectra. Figure 7 displays the S-wave acceleration spectra of the main event obtained for each station. This figure illustrates the attenuation effect on the S-wave amplitude spectra. At 1 Hz, for instance, the amplitude decreased four orders of magnitude between the station at epicenter distance of 205 km and the station at 659 km, in a 454-km interval. For detailed analysis, we calculated the geometric mean ( $a(f) = \sqrt{a_{NS}^2(f) + a_{EW}^2(f)}$ ) of the horizontal components of the S-wave amplitude spectra and the vertical component for the P wave.

We estimated site effects at the stations by calculating average spectral ratios between horizontal and vertical components of S waves (HVSr method). Since most stations of the array are located on hard-rock sites, we do not expect important amplifications, and the HVSr method can give a first-order estimate

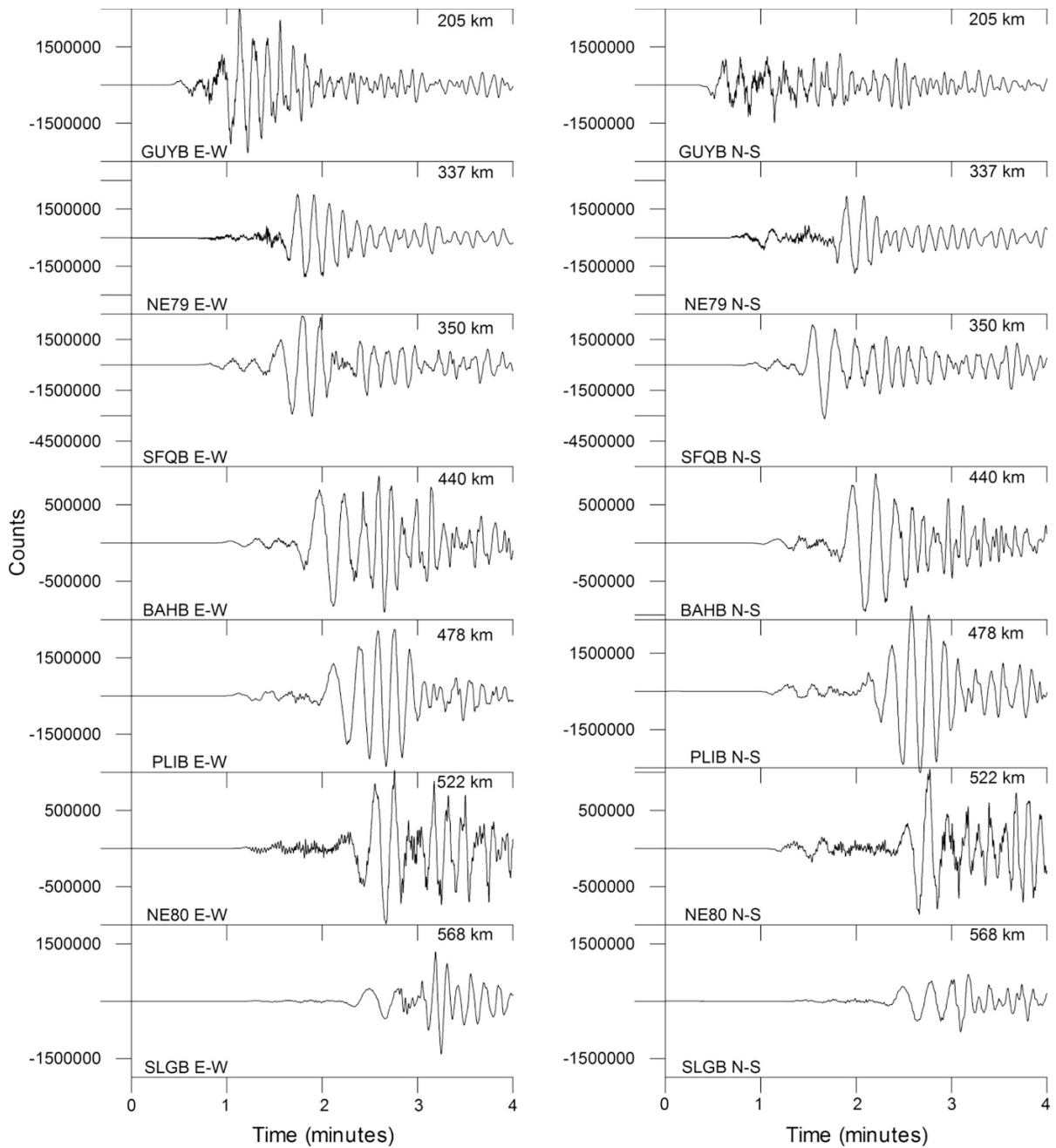


Figure 6

Horizontal component seismograms of main event of October 19, 2013 ( $M_w = 6.6$ ). The *left column* is the east–west component, while the *right column* is the north–south component of the RESBAN stations

of the site response. We used waveforms from the 2013 sequence and events recorded by the RESBAN array and the Network of Autonomously Recording Seismographs of Baja California, NARS-Baja,

(Trampert et al. 2003; Clayton et al. 2004) between 2002 and 2006, and analyzed previously by Avila-Barrientos and Castro (2015). We calculated for each station the spectral ratio between the horizontal and



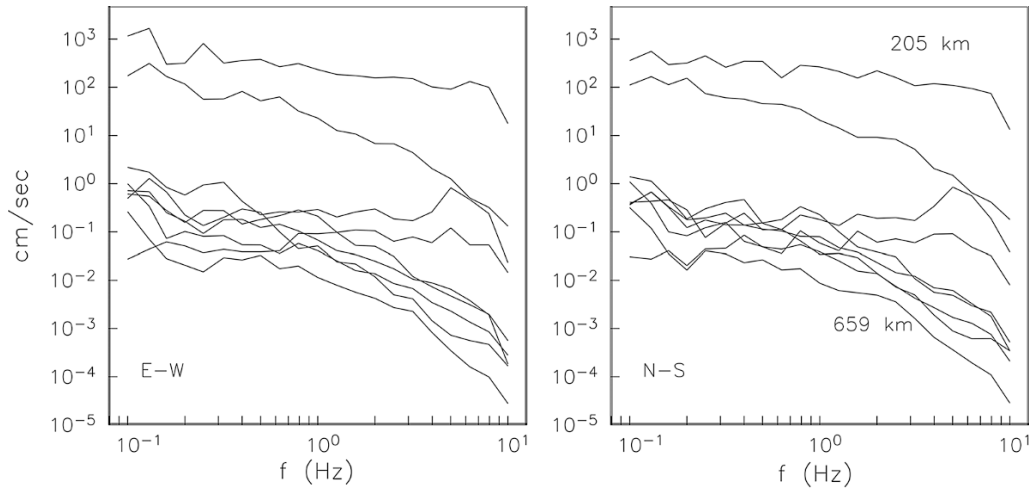


Figure 7

S-wave acceleration spectra of the main earthquake. *Left frame* are east–west components and *right frame* north–south components

vertical components (HVSR method) of each event. Then, we computed the average of all events and the geometric mean of both horizontal components. We assumed that the resulting average HVSR represents the site response of the corresponding station.

The HVSR method was originally proposed by Nakamura (1989) and extended by Lermo and Chávez-García (1993) to estimate the site amplification of the horizontal component of ground motion. This method assumes that the vertical component of the ground motion is insensitive to site amplification (Langston 1977; Nakamura 1989), so that when the spectral ratio between the horizontal and the vertical component is calculated, the source effect and any other path effect common for both components cancel out. The original S-wave spectra were corrected by site effect using the corresponding site response calculated with the HVSR method. The site-corrected spectra were then inverted to determine the source functions and to estimate the attenuation quality factor  $Q$  according to the following model:

$$U_i(r, f) = S_i(f) \cdot \frac{N}{r^n} \exp\left[-\frac{\pi f}{Qv}(r - N)\right], \quad (1)$$

where  $U_i(r, f)$  is the observed spectral amplitude after site effect correction at frequency  $f$  from event  $i$  recorded at hypocenter distance  $r$ .  $S_i(f)$  is the acceleration source function of event  $i$ ,  $\frac{N}{r^n}$  is the geometrical spreading function, with  $N = 10$  km

being a normalization factor. Vidales-Basurto et al. (2014) calculated the geometrical spreading exponent  $n$  in the GoC for both P and S waves and found that this exponent varies between 0.8 and 1.1 for P waves and between 0.8 and 1.0 for S waves. We make  $n = 0.9$  in Eq. (1).  $v$  is the wave velocity, we used a value of 3.77 km/s for S and 6.71 km/s for P waves.  $Q$  is the wave quality factor that accounts for both intrinsic and scattering attenuation. The estimates of  $Q$  are conditioned to the geometrical spreading function selected. However, the value of  $n = 0.9$  is very close to the expected theoretical value for body waves ( $n = 1$ ). Thus, the geometrical spreading function that we defined is a reasonable reference to estimate  $Q$ .

For a given frequency  $f$  and source-station distance  $r_j$ , Eq. (1) can be linearized by taking logarithms:

$$u_{ij} = s_i + cQ^{-1} \quad (2)$$

where:

$$u_{ij} = \text{Log}U_i(r, f) + 0.9\text{Log}r_j - 1.0 \quad (3)$$

$$s_i = \text{Log}S_i(f) \quad (4)$$

$$c = -\frac{\pi}{v}(r_j - 10)\text{Log}e \quad (5)$$

The estimates of  $Q$  resulting from the inversion of Eq. (2) can be used, in a second step, to recalculate

the S-wave site responses and to make new estimates of P-wave site responses. We corrected the original spectral records for attenuation effect with the same geometrical spreading function in Eq. (1) and the estimates of  $Q$  obtained solving Eq. (2). Thus, the observed spectral amplitude after attenuation effect correction at frequency  $f$  from event  $i$  at site  $j$  can be expressed as:

$$d_{ij} = s_i + z_j, \quad (6)$$

where  $s_i$  is the acceleration source function of event  $i$ , as in Eq. (4), and  $z_j = \text{Log}Z_j(f)$  represents the site

response of the station  $j$ . Equation (6) is solved by a least-squares inversion using the singular value decomposition technique (e.g. Castro et al. 1990).

A similar inversion technique has been used before by Phillips and Aki (1986) and Andrews (1986) to determine site effects and source functions in California. To eliminate the linear dependence between site and source terms, we used as a reference site the station that shows minimum HVSR values (station PPXB). The site and source terms in Eq. (6) are calculated independently at each frequency. The advantage of this method is that the stability of the

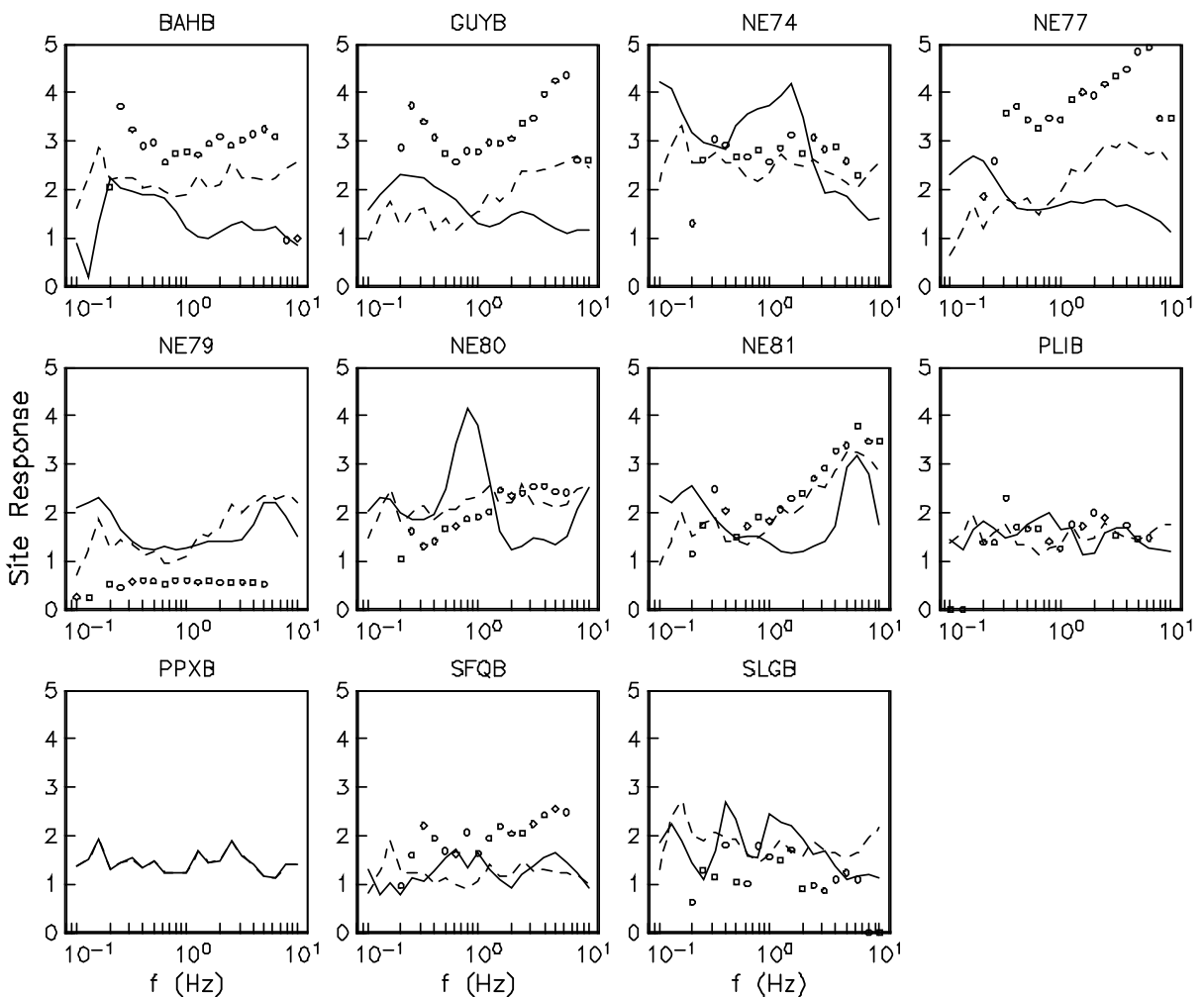


Figure 8

Site response of the stations analyzed. *Solid* and *dashed lines* are the S-wave responses obtained using horizontal-to-vertical spectral ratios (HVSR method) and the spectral inversion, respectively. The *small circles* are the P-wave responses resulting from the spectral inversion

Table 3

*Station coordinates and site geology of the RESBAN network*

Code	Latitude	Longitude	Elevation (m)	Group class	Site geology
BAHB	28.943	-113.561	35	I	Igneous intrusive: granodiorite-tonalite
PPXB	31.335	-113.632	10	I	Igneous intrusive: granite-granodiorite
PLIB	29.915	-112.694	40	I	Igneous intrusive: granodiorite
GUYB	27.899	-110.871	50	II	Igneous breach with fractures filled with calcium carbonate
NE74	28.008	-114.014	21	III	Eolian deposits unconsolidated composed of fine sands
NE77	26.016	-111.361	40	II	Sedimentary deposits and conglomerates
NE79	23.119	-109.756	225	I	Igneous intrusive: granite-granodiorite
NE80	30.500	-112.320	225	III	Unconsolidated sandstone
NE81	28.918	-109.636	295	III	Unconsolidated conglomerate
SFQB	28.405	-112.861	50	I	Igneous intrusive: granite
SLGB	29.830	-114.404	15	II	Volcanic breccia

Group I correspond to stations located on intrusive volcanic rocks with low degree of weathering; Group II are extrusive igneous rocks with moderate weathering; Group III are stations located on poorly consolidated conglomerates or soil

solutions is independent from the fall-off at high frequencies, since the shape of the source functions is unconstrained (e.g. Castro et al. 2013).

#### 4. Site Effects

The site functions calculated with the HVSR method (solid lines in Fig. 8) show small amplifications (less than a factor of two) at most frequencies. Stations NE74 and NE80, that are located on sand sediments (Table 3), have site amplifications that reach a factor of four at 1.6 and 0.7 Hz, respectively. Avila-Barrientos and Castro (2015) studied the site response at the stations of the RESBAN and NARS-Baja networks and classified the sites in three groups according to the near-surface geology below the stations. Group I corresponds to stations located on intrusive volcanic rocks with low degree of weathering; Group II are extrusive igneous rocks with moderate weathering; and Group III are stations located on poorly consolidated conglomerates or soil. Stations NE74, NE80 and NE81 are in the Group III, NE81 has its peak site amplification of three at 6 Hz, the likely natural frequency of resonance of this site. PPXB (Group I) is on a hard-rock outcrop (granite), and its site response function is approximately flat for the whole frequency band analyzed (0.10–10.0 Hz). We used PPXB as the reference site to solve Eq. (6) and the other site functions (solid lines in Fig. 8) to

correct the observed spectral records for site amplification effect and to determine Q and source functions solving Eq. (2). Figure 8 also shows the site responses obtained from the observed P-wave spectra (small circles) and from S-wave (dashed lines) solving Eq. (6). The site response from P waves is similar to that obtained from S waves solving Eq. (6), except for sites BAHB, GUYB and SFQB where the P-wave site amplification is higher. Sites with low S-wave amplification also tend to have low P-wave amplification, for instance NE79, PLIB and SLGB. Comparing the S-wave site responses obtained from the two methods (HVSR and Eq. (6)), we can see that Eq. (6) tends to give larger amplifications at high frequencies ( $f > 1$  Hz) at sites BAHB, GUYB, NE77, NE80 and SLGB. This may be an effect of using different site reference and number of events. For the HVSR method, there were more available events and records, and the possible azimuthal effects tend to average out better. Since the HVSR method assumes zero amplification on the vertical component, the lower S-wave amplification obtained with the HVSR between 1–10 Hz, compared to that obtained with the spectral inversion (Eq. (6)), could be due to S-wave amplification on the vertical component. For instance, Castro et al. (2004) observed in central Italy that sites located in sedimentary basins with thick sediments show important vertical amplifications at low frequencies. However, in general, HVSR gives a good estimate of the site



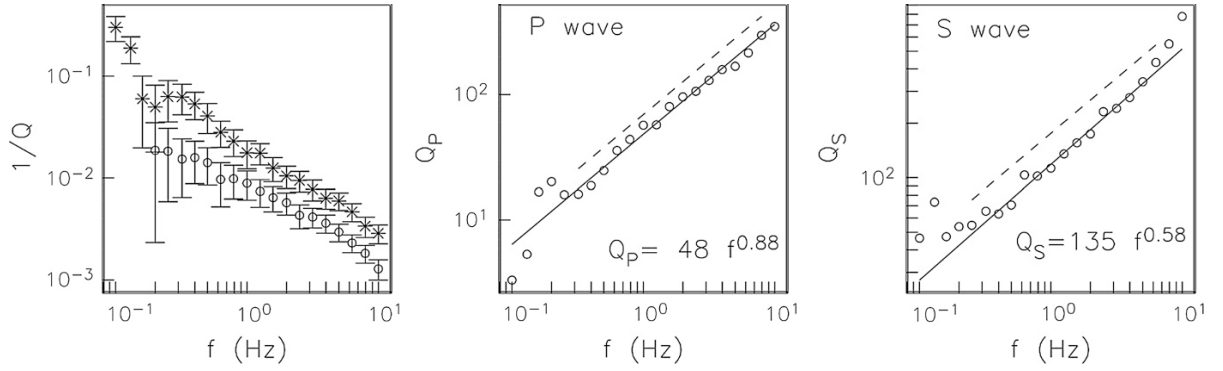


Figure 9

Estimates of the quality factor  $Q$  (left frame) obtained from the spectral inversion (asterisks for P and circles for S waves). The continuous line in the middle and right frames is the resulting linear regression of the  $Q$  estimates and the dashed lines the functions  $Q_P = 69 f^{0.87}$  and  $Q_S = 176 f^{0.61}$  obtained by Vidales-Basurto et al. (2014) for P and S waves, respectively, in the south-central region of the Gulf of California

response although tends to sub-estimate the amplifications at high frequencies. Similar results were obtained by Edwards et al. (2013) in Switzerland using regional seismicity.

### 5. P- and S-Wave Attenuation in the Gulf of California

We solved Eq. (2) for each of the 21 frequencies that sample the observed spectral records to estimate values of  $Q$  for P and S waves (Fig. 9). The values of  $Q$  for P waves ( $Q_P$ ) tend to be lower than those for S waves ( $Q_S$ ), indicating higher attenuation for compressional waves (left frame of Fig. 9) compared to shear waves. The frequency dependence of  $Q$  can be approximated with the functional form:

$$Q = Q_0(f/f_0)^a, \quad (6)$$

where  $Q_0$  is the value of  $Q$  at  $f_0 = 1.0$  Hz.

We found the following  $Q$ -frequency relations for P and S waves:

$$Q_P = 48.1 \pm 1.1f^{0.88 \pm 0.04} \quad (7)$$

$$Q_S = 135.4 \pm 1.1f^{0.58 \pm 0.03} \quad (8)$$

Seismic attenuation in the south-central region of the GoC was previously studied by Vidales-Basurto et al. (2014) with records from the NARS-Baja and RESBAN arrays, and from an array of ocean-bottom seismographs (OBS) deployed as part of the Sea of Cortez Ocean Bottom Array experiment (SCOOPA)

(Sumy et al. 2013). We compare in Fig. 9 their results (dashed lines) with those obtained in this study. Although the data set used by Vidales-Basurto et al. (2014) covers a bigger area, their  $Q$ -frequency functions show similar trends. However, their  $Q$  values are slightly higher for both P and S waves. It is also interesting to compare these values of  $Q$  with those reported inland, north of the GoC. For the Imperial Valley, California region, Singh et al. (1982) found that  $Q_S = 20f$ . Rebollar et al. (1985) estimated  $Q$  from coda waves in northern Baja California, and they found that  $Q_C = 37f^{0.87}$ . Raoof et al. (1999) found in southern California that  $Q_S = 180 f^{0.45}$  for frequencies between 0.25 and 5.0 Hz. Adams and Abercrombie (1998) used data from the Cajon Pass borehole to study  $Q$ , and they found that from 1 to 10 Hz,  $Q_S$  is frequency-dependent with an average total (intrinsic and scattering)  $Q_S = 1078$ .

The ratio  $Q_P/Q_S$  (Fig. 10) is below 1.0 in the whole frequency band 0.1–10 Hz. Experimental studies made in rocks indicate that when the rocks are partially saturated,  $Q_P/Q_S < 1$  and when the rocks are totally saturated,  $Q_P/Q_S > 1$  (Winkler and Nur 1982). These results suggest that the body-wave amplitudes are affected by partially saturated rocks probably associated to magmatic bodies located near the ridge zones. Hauksson and Shearer (2006) found that  $Q_S/Q_P > 1$  in southern California, suggesting that the crust is partially fluid-saturated in that region. They estimated that  $Q_P \sim 500\text{--}900$  and  $Q_S \sim 600\text{--}1000$  with a mean value of  $Q_P/Q_S = 0.77$ . In the Salton

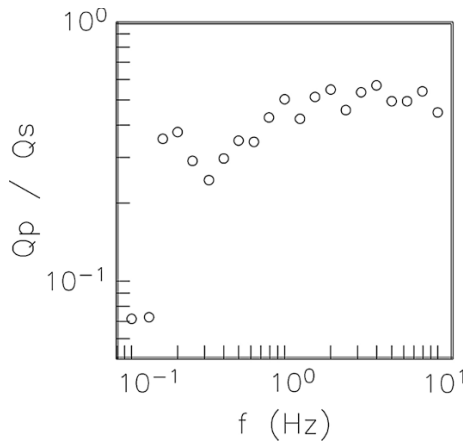


Figure 10

$Q_p/Q_s$  ratios calculated with the estimates of  $Q$  shown in Fig. 9

Trough region, Schlotterbeck and Abers (2001) reported that  $Q_p/Q_s = 1.43$ .

The seismic attenuation in the GoC has been also evaluated by Castro and Avila-Barrientos (2015) who calculated the spectral decay parameter kappa ( $\kappa$ ).  $\kappa$  measures the decay of high-frequency ground-motion amplitudes and is used for evaluating seismic risk and hazard.  $\kappa$ , as introduced by Anderson and Hough (1984), is controlled by the attenuation along the path and at the site. Castro and Avila-Barrientos (2015) found that  $\kappa$  near most sites of the RESBAN array have a value of  $\kappa_0 = 0.03$  s, except for station GUYB (Guaymas) which is located on a less-consolidated soil and has a  $\kappa_0 = 0.05$  s. They also found that at short distances (50–60 km),  $\kappa = 0.04$  for a station located in the middle of the array (NE76). Converting  $\kappa = 0.04$  s to  $Q_s$  ( $Q_s = \frac{r}{\beta\kappa}$ ), for  $r = 50$  km and  $\beta = 3.77$  km/s,  $Q_s = 332$ . This value of  $Q_s$  corresponds to a frequency of 4.7 Hz, from Eq. (8). The near-surface attenuation parameter  $\kappa_0$  is specific to each site (Anderson 1991) and can mask the source parameters, particularly the corner frequency. We account for the near-surface attenuation in this study by determining the site response function of each station used.

## 6. Source Functions

The acceleration source functions  $\pm 1$  SD resulting from the inversion of the observed acceleration spectra, after removing site effects (Eq. (2)) are

shown in Fig. 11. Source 1 is the foreshock that occurred on September 2, 2013, the main event of the sequence is source 2, and the rest of the sources are displayed chronologically according to the time of occurrence. As expected, the amplitudes of the acceleration source functions tend to increase at low frequencies (1–2 Hz), although the source amplitudes of the main event (source 2) are approximately constant for the whole frequency band. At high frequencies ( $f > 8$  Hz), the source amplitudes show a sudden decay, probably due to the near-source attenuation. Because the low sampling rate of the data and the narrow frequency band of this attenuation effect, we cannot quantify it. However, it is also possible that the observed high-frequency decay may be caused by the anti-alias filter that begins just before the Nyquist frequency of 10 Hz. We plotted the source functions between 0.1 and 8.0 Hz, to avoid the sampling rate effect, and observed that for events 2, 7, 9 and 10, the high-frequency decay persists. This suggests that a near-source attenuation effect is a possible explanation to the observed high-frequency decay of the source functions.

To estimate source parameters, we converted these functions into far-field source acceleration spectra  $f^2 \dot{M}_0(f)$  (e.g. Boore 1986)

$$f^2 \dot{M}_0(f) = \frac{\rho \beta^3 r}{1.4\pi \Re} S(f), \quad (9)$$

where  $\dot{M}_0(f)$  is the moment time derivative,  $\rho = 2.8$  g cm<sup>-3</sup>,  $\beta = 3.77$  km s<sup>-1</sup>,  $r = 10$  km (the reference distance) and an average radiation pattern  $\Re = 0.6$  for S waves. The factor of 1.4 accounts for the energy partition into two components and the free surface amplification.

The resulting far-field source acceleration spectra are displayed in Fig. 12 with solid lines. We fit these observed functions to the  $\omega^2$  model (Aki 1967; Brune 1970):

$$f^2 \dot{M}_0(f) = \frac{f^2 M_0}{1 + \left(\frac{f}{f_c}\right)^2} \quad (10)$$

The low-frequency level was fixed with the seismic moment ( $M_0$ ) calculated with the magnitude reported by the ISC catalog for each event, and the corner frequency ( $f_c$ ) was obtained by trial and error

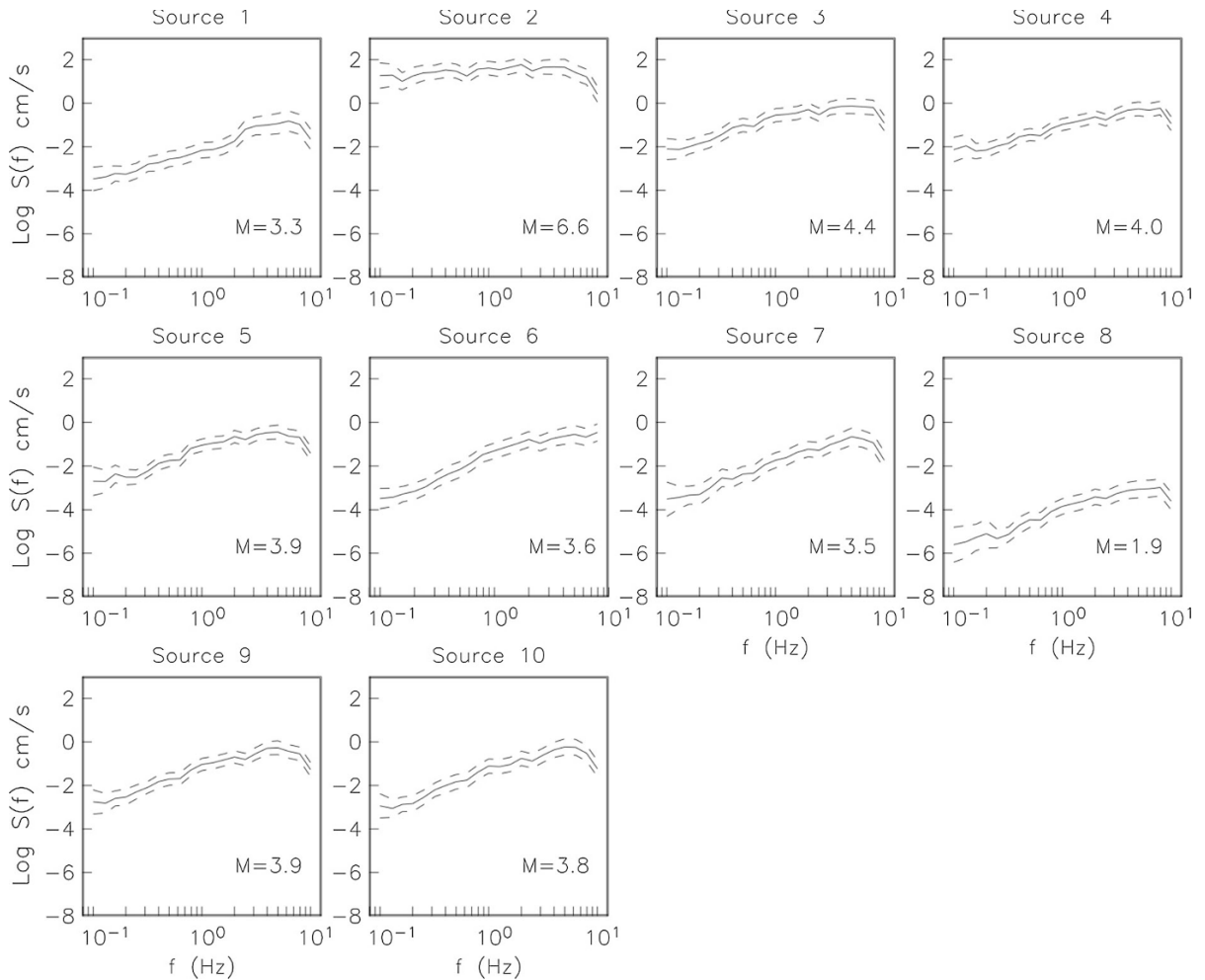


Figure 11  
Source functions ( $\pm 1$  SD) resulting from the spectral inversion

testing all possible values from 0.1 to 10.0 Hz with increments of 0.001 Hz. The magnitudes reported by ISC for the sources 2, 4 and 9 fit well the low-frequency part of the spectra. For event 3, we used the magnitude ( $M$  4.4) reported by the Mexican Seismological Service (SSN), which is in between the magnitudes reported by the ISC catalog. The SSN estimated a magnitude  $M = 3.8$  for event 8 but is not listed in the ISC catalog, suggesting that perhaps the actual magnitude of this event is below the minimum magnitude of completeness of the ISC catalog. The low-frequency level of the source functions of events 1, 5, 6, 7 and 8 cannot be fit with the  $\omega^2$  model with

the  $M_0$  estimated with the reported magnitudes. We calculated  $M_0$  of these earthquakes with the observed low-frequency level  $\Omega_0$ , and the corner frequency was recalculated.

We used the corner frequency that gives the smaller residual between the  $\omega^2$  model and the observed source spectra to estimate the stress drop with the Brune (1970) model:

$$\Delta\sigma = \frac{7}{16} \frac{M_0 f_c^3}{(0.37\beta)^3} \quad (11)$$

We estimate a stress drop of 1.7 MPa for the mainshock and smaller values for the aftershocks and



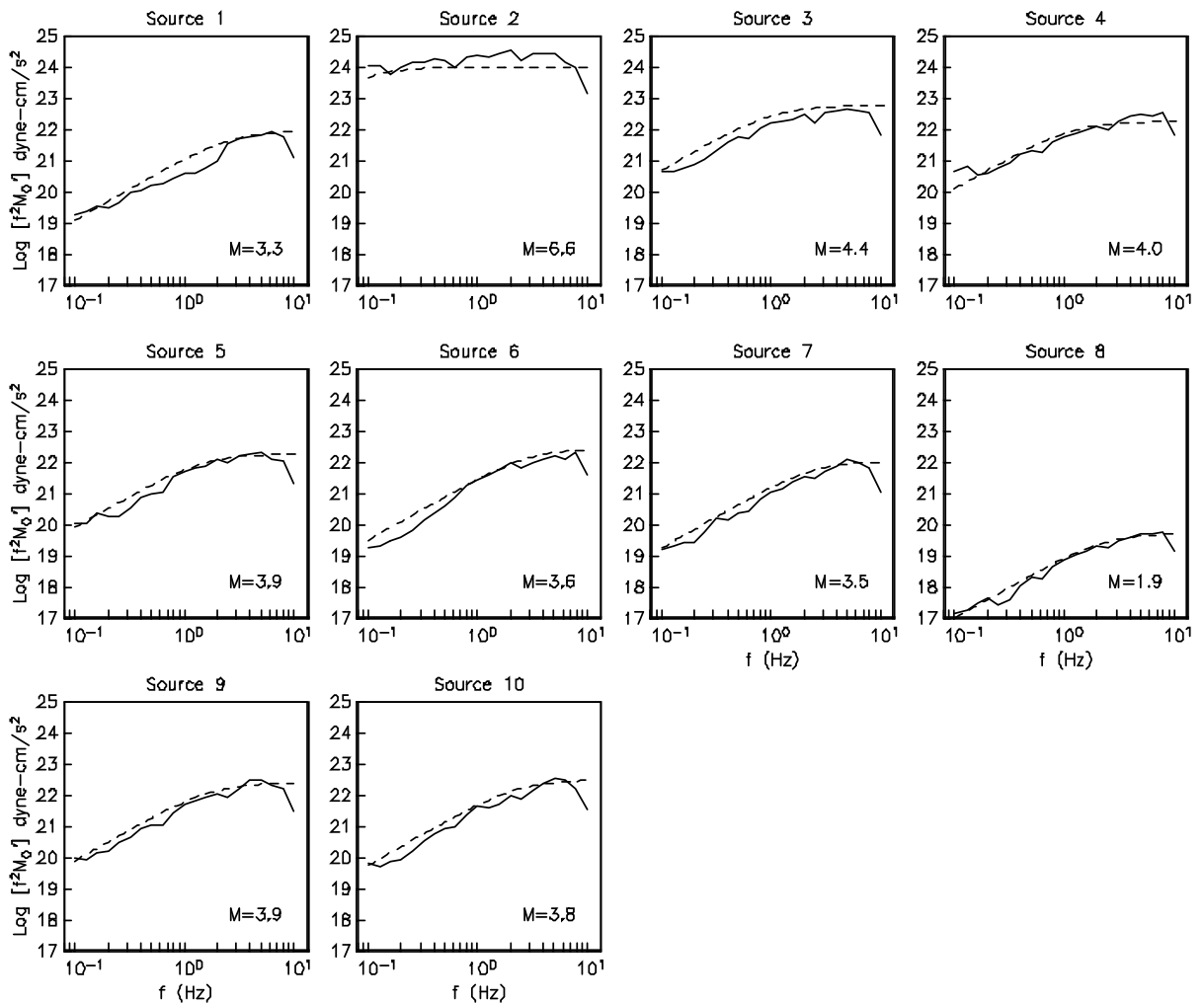


Figure 12

S-wave far-field acceleration source functions (*continuous line*) and the best fits of the Brune's  $\omega^2$  model (*dashed lines*)

the foreshock (Table 4). In general, the stress drops of this sequence are between 0.34 and 1.7 MPa, except for event 8, the smallest of all ( $M_w$  1.9) that has a stress drop of 0.002 MPa (Fig. 13). We expect values of  $f_c$  in the range of 5–10 Hz for events with magnitudes  $M_w \sim 2.0$  (e.g. Van Houtte et al. 2014). Because the low magnitude of this event, it is possible that the corner frequency may be close or above 10 Hz, outside the useful frequency band of the data, and our estimate of the stress drop is likely inaccurate for this event. We prefer to ignore the results from event 8 for further analyses.

## 7. Discussion and Conclusions

Although the foreshock, the main event and most aftershocks of the sequence occurred on the Farallon transform fault, several aftershocks are located near the ridge that separates Carmen and Farallon transform faults (Fig. 2). The foreshock (event 1) is located on the northern end of the Farallon fault and the mainshock 55 km to the southeast and SE of the rift. The rupture propagated NW for approximately 27 km, triggering earthquakes on the ridge zone and on the Carmen transform fault, 17 km north of the

Table 4

Source parameters estimated with the  $\omega^2$  model

Event no.	Fault	$M_0$ (N-m)	$f_c$ (Hz)	Stress drop (MPa)	$r_s$ (km)	$M$	Refs.
1	Farallon	0.1234E15	2.68	0.38	0.52	3.3	1
2	Farallon	0.8921E19	0.11	1.71	13.25	6.6	2
3	Ridge	0.4955E16	1.08	1.00	1.30	4.4	3
4	Farallon	0.1245E16	1.20	0.34	1.17	4.0	2
5	Farallon	0.8264E15	1.50	0.45	0.94	3.9	1
6	Ridge	0.3141E15	2.95	1.29	0.48	3.6	1
7	Carmen	0.1766E15	2.47	0.43	0.57	3.5	1
8	–	0.9931E12	2.28	0.002	0.62	1.9	1
9	Farallon	0.7889E15	1.77	0.71	0.79	3.9	2
10	Ridge	0.5585E15	2.34	1.16	0.60	3.8	1

$M_0$  is the seismic moment,  $f_c$  the corner frequency and  $r_s$  the source radius. The last column (Ref) indicates the source of the magnitude values: 1 from the seismic moment calculated with the observed low-frequency spectral level  $\Omega_0$ ; 2 from the ISC catalog; 3 from the Mexican Seismological Service catalog

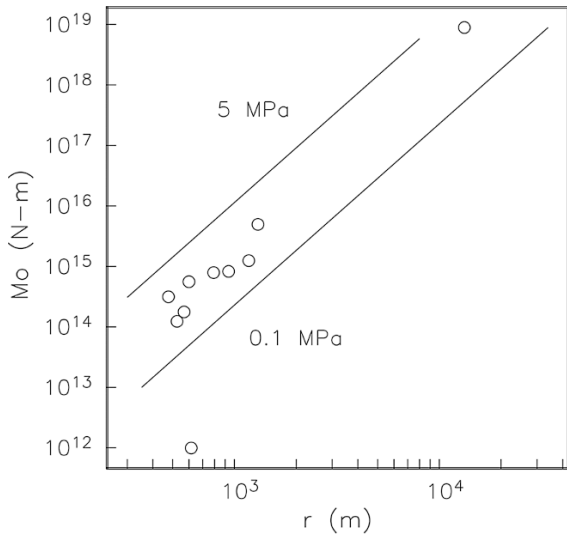


Figure 13

Seismic moment versus source radius obtained fitting the far-field source functions with the Brune's model. We estimated a stress drop of 1.7 MPa for the main event ( $M_w$  6.6) and 0.002 MPa for the smaller aftershock ( $M$  1.9)

Farallon fault trace. The bathymetry and the location of one of the aftershocks (event 6 in Fig. 2 and Table 2) suggest that the Carmen fault continues (SE) beyond the ridge for at least 23 km, contrary to the expected geometry of a typical en echelon transform fault system where the ridge zone marks the end of the fault and jumps to the other end of the ridge. The character of the Farallon transform fault looks smoother to the SE of the 2013 earthquake sequence,

and that is probably why the 2013 sequence was located on the NW section, where the transform fault is more geometrically complicated, and it likely has more off-fault deformation, which would account for the epicentral distribution of the aftershocks.

The estimates of site response obtained with the HVSR method indicate that most stations of the RESBAN network have low site amplifications; however, stations NE74, NE80 and NE81 show significant site response amplifications that are above a factor of 3 (Fig. 8). The S-wave site responses obtained with HVSR tend to give larger amplifications at high frequencies ( $f > 1$  Hz) at sites BAHB, GUYB, NE77, NE80 and SLGB compared with the S-wave responses estimated with the source-site spectral inversion (solving Eq. (6)). This may be an effect of azimuthal dependence of the site response. The site responses from P waves are similar to those obtained from S waves, except for sites BAHB, GUYB and SFQB where the P-wave site amplification is higher. These three stations are located on hard-rock sites (igneous rocks) and show small S-wave site amplifications (Fig. 8).

The frequency dependence of the quality factor of S waves can be approximated with the relation  $Q_s = 135.4 \pm 1.1f^{0.58 \pm 0.03}$  ( $0.1 \leq f \leq 10$ ), which is consistent with previous estimates by Vidales-Basurto et al. (2014) obtained for the south-central region of the Gulf of California. Similarly, for P waves, we find the relation  $Q_p = 48.1 \pm 1.1f^{0.88 \pm 0.04}$ . The ratio  $Q_p/Q_s < 1.0$  found in the frequency band 0.1–10 Hz

(Fig. 10) suggests that partially saturated rocks may be present along the wave propagation paths. These zones of low  $Q_P/Q_S$  may be related to magmatic bodies located near the ridges.

We estimate that the October 19, 2013 ( $M_w$  6.6) earthquake has a stress drop of 1.7 MPa. Aftershocks 3, 6 and 10 (Table 4), located near the ridge, also show the highest stress drops (Fig. 2). The seismicity reported by Sumy et al. (2013) in the Farallon–Carmen regions (Fig. 4) tends to concentrate near the ridges, suggesting that the interaction of the Farallon and Carmen transform faults may concentrate stress in between, near the ridge, where the higher stress drop earthquakes of the 2013 sequence occurred.

### Acknowledgments

The operation of the RESBAN network has been possible thanks to the financial support of the Mexican National Council for Science and Technology (CONACYT) (projects CB-2011-01-165401(C0C059), G33102-T and 59216). This paper was prepared while the first author (RRC) was on sabbatical year in Caltech. We thank Prof. Gurnis for the support provided. Dr. Lenin Avila-Barrientos facilitated part of the spectral records used to calculate the site functions. Antonio Mendoza Camberos pre-process the data from the RESBAN network and Arturo Perez Vertti maintains and operates the stations. We thank Dr. Edwards and the anonymous reviewer for their careful revisions, comments and suggestions which help us to improve the manuscript. We also acknowledge the Editor, Dr. Thomas H.W. Goebel.

### REFERENCES

- Adams, D. A., & Abercrombie, R. E. (1998). Seismic attenuation above 10 Hz in southern California from coda waves recorded in the Cajon Pass borehole. *Journal Geophysical Research*, *103*, 24257–24270.
- Aki, K. (1967). Scaling law of seismic spectrum. *Journal Geophysical Research*, *72*, 1217–1231.
- Anderson, J. G. (1991). A preliminary descriptive model for the distance dependence of the spectral decay parameter in southern California. *Bulletin of the Seismological Society of America*, *81*, 2186–2193.
- Anderson, J. G., & Hough, S. E. (1984). A model for the shape of the Fourier amplitude spectrum of acceleration at high frequencies. *Bulletin of the Seismological Society of America*, *74*, 1969–1993.
- Andrews, D.J. (1986). Objective determination of source parameters and similarity of earthquakes of different size. In S. Das, J. Boatwright, C. H. Sholz (Eds.) *Earthquake source mechanics*. Washington, DC: American Psychological Union. doi:10.1029/GM037p0259
- Atwater, T., & Stock, J. (1998). Pacific-North America plate tectonics of the Neogene Southwestern United States: An update. *International Geology Review*, *40*, 375–402.
- Avila-Barrientos, L., & Castro, R. R. (2015). Site response of the NARS-Baja and RESBAN broadband networks of the Gulf of California, Mexico. *Geofísica Internacional*, *55*, 131–154.
- Boore, D. M. (1986). Short-period P- and S-wave radiation from large earthquakes: implications for spectral scaling relations. *Bulletin of the Seismological Society of America*, *76*, 43–64.
- Brune, J. N. (1970). Tectonic stress and the spectra of seismic shear waves from earthquake. *Journal Geophysical Research*, *75*, 4997–5009.
- Carbotte, S. M., Arko, R., Chayes, D. N., Haxby, W., Lehnert, K., O'Hara, S., et al. (2004). New integrated data management system for Ridge 2000 and MARGINS research. *EOS Transactions, AGU*, *85*(51), 553. doi:10.1029/2004EO510002.
- Caress, D. W., & D. N. Chayes. (2014). MB-System: Mapping the Seafloor. <https://www.mbari.org/data/mbsystem> and <http://www.ideo.columbia.edu/res/pi/MB-System>. Accessed 4 Jan 2016
- Castro, R. R., Anderson, J. G., & Singh, S. K. (1990). Site response, attenuation and source spectra of S waves along the Guerrero, México, subduction zone. *Bulletin of the Seismological Society of America*, *80*, 1481–1503.
- Castro, R. R., & Avila-Barrientos, L. (2015). Estimation of the spectral parameter kappa in the region of the Gulf of California, Mexico. *Journal of Seismology* *19*, 809–829. doi:10.1007/s10950-015-9496-x.
- Castro, R. R., Pacor, F., Bindi, D., Franceschina, G., & Luzi, L. (2004). Site response of strong motion stations in the Umbria, Central Italy, region. *Bulletin of the Seismological Society of America*, *94*, 576–590.
- Castro, R. R., Pacor, F., Puglia, R., Ameri, G., Letort, J., Massa, M., & Luzi, L. (2013). The 20 May, 2012 Emilia earthquake, Italy and the main aftershocks: S-wave attenuation, acceleration source functions, and site effects. *Geophysical Journal International*, doi:10.1093/gji/ggt245.
- Castro, R. R., Pérez-Vertti, A., Mendez, I., Mendoza, A., & Inzunza, L. (2011a). Location of moderate size earthquakes recorded by the NARS-Baja array in the Gulf of California region between 2002 and 2006. *Pure and Applied Geophysics*, *168*, 1279–1292.
- Castro, R. R., Valdes-Gonzalez, C., Shearer, P., Wong, V., Astiz, L., Vernon, F., et al. (2011b). The 3 August 2009  $M_w$  6.9 Canal de Ballenas region, Gulf of California, earthquake and its aftershocks. *Bulletin of the Seismological Society of America*, *101*, 929–939.
- Clayton, R. W., Trampert, J., Rebolgar, C. J., Ritsema, J., Persaud, P., Paulssen, H., et al. (2004). The NARS-Baja array in the Gulf of California Rift Zone. *Margins Newsletter*, *13*, 1–4.
- Edwards, B., Michel, C., Poggi, V., & Fah, D. (2013). Determination of site amplification from regional seismicity: Application to the Swiss National Seismic Networks. *Seismological Research Letters*, *84*, 611–621. doi:10.1785/0220120176.



- Fenby, S. S., & Gastil, R.G. (1991). Geologic-Tectonic map of the Gulf of California and surrounding áreas. In J. P. Dauphin & B. T. Simoneit (Eds.), *The Gulf and Penninsular provinces of the Californias* (Vol. 47, pp. 79–83). Tulsa: American Association of Petroleum Geologist.
- Goff, J. A., Bergman, E. A., & Solomon, S. C. (1987). Earthquake source mechanism and transform fault tectonics in the Gulf of California. *Journal Geophysical Research*, 92, 10485–10510.
- Hauksson, E., & Shearer, P. M. (2006). Attenuation models ( $Q_P$  and  $Q_S$ ) in three dimensions of the southern California crust: Inferred fluid saturation at seismogenic depths. *Journal Geophysical Research*, 111, B05302. doi:10.1029/2005JB003947.
- Langston, C. A. (1977). Corvallis, Oregon, crustal and upper mantle receiver structure from teleseismic P and S waves. *Bulletin of the Seismological Society of America*, 67, 713–724.
- Lermo, J., & Chávez-García, F. J. (1993). Site effect evaluation using spectral ratios with only one station. *Bulletin of the Seismological Society of America*, 83, 1574–1594.
- Lizarralde, D., Axen, G. J., Brown, H. E., Fletcher, J. M., Gonzalez-Fernandez, A., Harding, A. J., et al. (2007). Variation in styles of rifting in the Gulf of California. *Nature*,. doi:10.1038/nature06035.
- Lonsdale, P. F. (1989). Geology and tectonic history of the Gulf of California. *The Eastern Pacific Ocean and Hawaii, Decade of North American geology* (Vol. N, pp. 499–521). Denver, CO, USA: Geol. Soc. Am.
- López-Pineda, L., & Rebolgar, C. J. (2005). Source characteristics of the  $M_w$  6.2 Loreto earthquake of 12 march 2003 that occurred in a transform fault in the middle of the Gulf of California, Mexico. *Bulletin of the Seismological Society of America*, 95, 419–430.
- Munguía, L., Reichle, M., Reyes, A., Simons, R., & Brune, J. (1977). Aftershocks of the 8 July, 1975 Canal de las Ballenas, Gulf of California, earthquake. *Geophysical Research Letters*, 4, 507–509.
- Nagy, E. A., & Stock, J. M. (2000). Structural control on the continent-ocean transition in the Northern Gulf of California. *Journal Geophysical Research*, 105, 16251–16269.
- Nakamura, Y. (1989). A method for dynamic characteristics estimation of subsurface using microtremor on the ground surface. *Report Railway Technical Research Institute*, 30, 25–33.
- Nava-Sánchez, E. H., Gorsline, D. S., & Molina-Cruz, A. (2001). The Baja California peninsula borderland: structural and sedimentological characteristics. *Sedimentary Geology*, 144, 63–82. doi:10.1016/S0037-0738(01)00135-X.
- Pacheco, J. F., & Sykes, L. R. (1992). Seismic moment catalog of large shallow earthquakes, 1900 to 1989. *Bulletin of the Seismological Society of America*, 82, 1306–1349.
- Phillips, W. S., & Aki, K. (1986). Site amplification of coda waves from local earthquakes in central California. *Bulletin of the Seismological Society of America*, 76, 627–648.
- Raoof, M., Hermann, R. B., & Malagnini, L. (1999). Attenuation and excitation of three-component ground motion in southern California. *Bulletin of the Seismological Society of America*, 89, 888–902.
- Rebolgar, C. J., Quintanar, L., Castro, R. R., Day, S. M., Madrid, J., Brune, J. N., et al. (2001). Source characteristics of a 5.5 magnitude earthquake that occurred in the transform fault system of the Delfin Basin in the Gulf of California. *Bulletin of the Seismological Society of America*, 91, 781–791.
- Rebolgar, C. J., Traslosheros, C., & Alvarez, R. (1985). Estimates of seismic wave attenuation in northern Baja California. *Bulletin of the Seismological Society of America*, 75, 1371–1382.
- Rodriguez-Lozoya, H. E., Quintanar, L., Ortega, R., Rebolgar, C. J., & Yagi, Y. (2008). Rupture process of four medium-size earthquakes that occurred in the Gulf of California. *Journal Geophysical Research*, 113, B10301. doi:10.1029/2007JB005323.
- Schlotterbeck, B. A., & Abers, G. A. (2001). Three-dimensional attenuation variations in southern California. *Journal Geophysical Research*, 106, 30719–30735.
- Singh, S. K., Apse, R. J., Fried, J., & Brune, J. N. (1982). Spectral attenuation of SH waves along the Imperial fault. *Bulletin of the Seismological Society of America*, 72, 2003–2016.
- Stein, S., & Pelayo, A. (1991). Seismological constraints on stress in the oceanic lithosphere. *Philosophical Transactions of the Royal Society of London A*, 337, 53–72.
- Stock, J. M., & Hodges, K. V. (1989). Pre-Pliocene extension around the Gulf of California and the transfer of Baja California to the Pacific plate. *Tectonics*, 8, 99–115.
- Sumy, D. F., Gaherty, J. B., Kim, W.-Y., Diehl, T., & Collins, J. A. (2013). The mechanism of earthquakes and faulting in the southern Gulf of California. *Bulletin of the Seismological Society of America*, 103, 487–506.
- Tanioka, Y., & Ruff, L. (1997). Source time functions. *Seismological Research Letters*, 68, 386–400.
- Trampert, J., Paulsen, H., Van Wettum, A., Ritsema, J., Clayton, R., Castro, R., et al. (2003). New array monitors seismic activity near the Gulf of California in México, EOS. *Transactions American Geophysical Union*, 84, 29–32.
- Van Houtte, C., Ktenidou, O. J., Larkin, T., & Holden, C. (2014). Hard-site  $\kappa_0$  (Kappa) calculations for Christchurch, New Zealand, and comparison with local ground motion prediction models. *Bulletin of the Seismological Society of America*, 104, 1899–1913.
- Vidales-Basurto, C. A., Castro, R. R., Huerta, C. I., Sumy, D. F., Gaherty, J. B., & Collins, J. A. (2014). An attenuation study of body-waves in the south-central region of the Gulf of California, México. *Bulletin of the Seismological Society of America*, 104, 2027–2042.
- Wessel, P., & Smith, W. H. F. (1998). New, improved version of generic mapping tools released. *EOS Transactions, AGU*, 79(47), 579.
- Winkler, K. W., & Nur, A. (1982). Seismic attenuation: effects of pore fluids and frictional sliding. *Geophysics*, 47, 1–15.
- Zhang, X., Paulsen, H., Lebedev, S., & Meier, T. (2007). Surface wave tomography of the Gulf of California. *Geophysical Research Letters*, 34, L15305. doi:10.1029/2007GL030631.

(Received January 25, 2016, revised June 27, 2016, accepted June 29, 2016, Published online July 9, 2016)